# FSM: A Reflectance Reconstruction Method to Retrieve Full-Spectrum Sun-Induced Chlorophyll Fluorescence From Canopy Measurements

Shilei Li, *Member, IEEE*, Maofang Gao, *Senior Member, IEEE*, Zhao-Liang Li, *Fellow, IEEE*, Jélila Labed, and Wouter Verhoef

***Abstract*— Full-spectrum Sun-induced chlorophyll fluorescence (SIF) offers profound physiological insights into plant functional status compared to single-band SIF. We propose a Fourier series-based method (FSM) for retrieving full-spectrum SIF, aiming to address the limitations of existing methods, such as reliance on reflectance training datasets and the limited spectral range of retrieved SIF spectrum. The core principle of the FSM involves modeling reflectance as a wavelength-dependent function, which can be approximated by successive summations using high-order expansions of the Fourier series. The performance of the FSM was thoroughly evaluated through a combination of simulations and field measurements. The findings illustrate FSM's capability to achieve high-precision full-spectrum SIF retrieval, with an average relative root-mean-square error (RRMSE) of 2.468% based on synthetic data. Moreover, the corresponding RRMSE values in the $O_2$-A and $O_2$-B bands, at 1.1% and 3.724%, respectively, indicate accuracy comparable to the spectral fitting method (SFM) and advanced FSR (aFSR) methods and superior to the SpecFit method. In the field full-spectrum SIF retrieval, FSM exhibited improved reflectance reconstruction and produced more reasonable results for the diurnal variation of full-spectrum SIF. The diurnal comparison of single-band SIF at both Italian and German sites further highlights the close alignment between FSM-retrieved SIF and the SFM SIF, with $R^2$ values exceeding 0.96 and a maximum RMSE of 0.118 mW/m$^2$/sr/nm. Conversely, the aFSR method encountered challenges stemming from an under-representation of the training dataset, resulting in the maximum RMSE at the Italian site reaching 0.506 mW/m$^2$/sr/nm, along with a minimum $R^2$ of 0.809. The FSM demonstrates the promising potential for full-spectrum SIF retrieval, accompanied by fewer limitations.**

***Index Terms*— Fourier series, full-spectrum Sun-induced chlorophyll fluorescence (SIF), MODTRAN, SCOPE, SIF retrieval, T-18 system.**

Received 22 March 2024; revised 22 June 2024 and 8 October 2024; accepted 11 October 2024. Date of publication 24 October 2024; date of current version 13 December 2024. This work was supported in part by the National Key Research and Development Program of China under Grant 2022YFD1500204, in part by the National Natural Science Foundation of China under Grant 41921001, and in part by the National Scholarship Fund of China under Grant 202103250059. *(Corresponding author: Maofang Gao.)*

Shilei Li and Zhao-Liang Li are with the State Key Laboratory of Efficient Utilization of Arid and Semi-Arid Arable Land in Northern China, Institute of Agricultural Resources and Regional Planning, Chinese Academy of Agricultural Sciences, Beijing 100081, China, and also with ICube, CNRS, Université de Strasbourg, Illkirch, 67412 Strasbourg, France (e-mail: lishilei@caas.cn; lizhaoliang@caas.cn).

Maofang Gao is with the State Key Laboratory of Efficient Utilization of Arid and Semi-Arid Arable Land in Northern China, Institute of Agricultural Resources and Regional Planning, Chinese Academy of Agricultural Sciences, Beijing 100081, China (e-mail: gaomaofang@caas.cn).

Jélila Labed is with ICube, CNRS, Université de Strasbourg, Illkirch, 67412 Strasbourg, France (e-mail: labed@unistra.fr).

Wouter Verhoef, retired, was with the Faculty of Geo-Information Science and Earth Observation (ITC), University of Twente, 7500 AE Enschede, The Netherlands. He resides in 8301 Emmeloord, The Netherlands (e-mail: w.verhoef@utwente.nl).

Digital Object Identifier 10.1109/TGRS.2024.3485576

## Nomenclature

| Parameters | Description |
|---|---|
| $E_o(b)$ | Irradiance in the direction of canopy observation. |
| $E_t$ | Irradiance at the top of atmosphere. |
| $\cos\theta$ | Cosine of solar zenith angle. |
| $\tau_{ss}$ | Direct atmospheric transmittance from the sun to the ground. |
| $\tau_{sd}$ | Diffuse atmospheric transmittance from the sun to the ground. |
| $\rho_{dd}$ | BOA spherical albedo of the atmosphere. |
| $F$ | SIF from the target. |
| $\overline{F_d}$ | Equivalent hemispherical SIF radiance from surroundings. |
| $r_{so}$ | Surface bidirectional reflectance factor. |
| $\overline{r_{sd}}$ | Spatially averaged directional-hemispherical reflectance over surroundings. |
| $\overline{r_{dd}}$ | Spatially averaged bi-hemispherical reflectance over surroundings. |
| $r_{do}$ | Surface hemispherical-directional reflectance for diffuse incidence. |

## I. Introduction

SUN-INDUCED chlorophyll fluorescence (SIF) has garnered widespread research interest over the past decade. SIF represents the spectral signal emitted by vegetation in response to solar radiation, typically ranging in wavelength from 650 to 850 nm. SIF has been broadly investigated, not only for its close correlation with gross primary production (GPP) at site-specific [1], [2], regional [3], [4], [5], and global scales [6], [7], [8] but also in scenarios relating to drought [9], vegetation phenology [10], and crop yield prediction [11].

Remote sensing of SIF presents certain challenges, as it is considered to be a component superimposed on the recorded upwelling radiance, with a relatively small contribution. Since the inception of the Fraunhofer line depth (FLD) principle [12], a succession of associated refinement algorithms has been developed, such as the three-band FLD (3FLD) method [13], the improved FLD (iFLD) method [14], and the PCA-based FLD (pFLD) method [15]. The essence of these methods lies in employing diverse approaches to characterize the relationship between reflectance and fluorescence inside and outside the absorption lines, thus enabling SIF retrieval at specific wavelengths. The spectral fitting methods (SFMs) employ smooth mathematical functions to describe the relationship between reflectance and fluorescence within the retrieval window [16], which, in theory, better represents the real scenario and thus also used as the reference retrieval method for SIF observation systems [17], [18].

Although the aforementioned methods have demonstrated favorable outcomes in SIF retrieval, it is worth noting that their measurements are confined to several discrete absorption lines. Research findings suggest that analyzing the full spectrum of SIF provides more detailed insights into plant characteristics than focusing on single bands. Specifically, the ratio of SIF emissions between the red and far-red regions has been found to correlate closely with chlorophyll content [19], nitrogen deficiency [20], and canopy light use efficiency over the diurnal cycle [21]. In addition, Verrelst et al. [22] exhibited the enhanced correlation between SIF and net photosynthesis of the canopy when employing a wide SIF spectrum (650–790 nm), as opposed to utilizing SIF at only one or few specific wavelengths. Furthermore, Mohammed et al. [23] emphasized the significance of full-spectrum SIF for future inquiries into fluorescence in relation to various canopy species, chemical and physical parameters, and physiological aspects. Familiarity with the complete fluorescence spectrum could prove advantageous in accurately measuring light reabsorption within a canopy, determining the distinct contributions of Photosystems I and II, and evaluating the fluorescence quantum efficiency. Therefore, it is imperative to conduct comprehensive research on full-spectrum SIF retrieval, as it possesses the capacity to further enhance the prospects of SIF applications. Several canopy full-spectrum SIF retrieval methods have been developed, encompassing the fluorescence spectrum reconstruction (FSR) [24], full-spectrum SFM (F-SFM) [25], SpecFit [26], and advanced FSR (aFSR) methods [27]. The performance of these methods was systematically compared and evaluated in [27], with results indicating the superiority of the aFSR method. However, it is crucial to acknowledge that the effectiveness of the aFSR method partially depends on the representativeness of the training data, as the method leverages dominant characteristics from the training dataset for accurate reflectance reconstruction.

In this study, we introduce a Fourier series-based method (FSM) for the retrieval of full-spectrum SIF, with the objective of addressing the limitations of existing retrieval methods, such as reliance on the availability reflectance training datasets and the limited spectral range of retrieved SIF spectrum. The performance of the FSM is assessed through coupled simulations under various atmospheric conditions and field measurements recorded using the FloX instruments. To ensure comprehensive comparisons, we employed the SFM, aFSR, and SpecFit methods for SIF retrieval, assessing both single-band and full-spectrum SIF results obtained from the FSM.

## II. MATERIALS

### A. Field Measurements

The field data utilized in this study were collected using the FloX monitoring field spectrometer, a highly automated instrument produced by JB-Hyperspectral Devices, located in Düsseldorf, Germany. This device is designed to capture both downwelling irradiance and upwelling radiance, equipped with optics that offer a hemispherical (∼180°) field of view for the former and a conical (∼25°) field of view for the latter. The FloX spectrometer operates within a spectral range of 650–800 nm and is characterized by a spectral resolution (SR) of 0.3 nm, alongside a spectral sampling interval of 0.17 nm. In addition, the system is capable of achieving a maximum signal-to-noise ratio (SNR) of 1000, demonstrating its high precision in spectral data acquisition.

The FloX system installations are positioned in Grosseto, Italy (43°55′48″N, 5°42′36″E) and Julich, Germany (50°52′12″N, 6°26′24″E). The observation targets include both Alfalfa, representing dense vegetation, and cover crop as an example of sparse vegetation, with observation heights of 1.5 and 3 m, respectively. In this study, we employed six instances of clear-sky observations collected on April 7, 16, and 25, 2018, in Italy, and on November 5, 7, and 18, 2020, in Germany. These spectral datasets are already publicly available on the online platform Zenodo (https://zenodo.org/records/7040578). For a more detailed description, please refer to the work by Naethe et al. [17].

Fig. 1 presents diurnal variations in upwelling radiance and apparent reflectance captured over six distinct days. The data from Italy, represented in the first two rows, illustrate the target vegetation's active growth phase, evidenced by a progressive increase in both radiance and apparent reflectance with each subsequent observation date. Conversely, the data from Germany, detailed in the last two rows, reflect a slower vegetation growth rate, attributable to the onset of winter. This is characterized by a modest rise in both radiance and apparent reflectance values. Collectively, the measurements from Italy and Germany comprise 1183 and 564 spectral cases, respectively.

### B. Synthetic Data

Synthetic data were generated through the integration of the SCOPE (version 2.1) and MODTRAN (version 5.2.2) models within the T-18 system framework [28], [29]. This integration of the SCOPE [30], [31] and MODTRAN [32] models has been extensively employed in research related to SIF retrieval [33], [34], [35]. The T-18 system enhances realism in data simulations by overcoming the simplistic assumption of a uniform Lambertian Earth surface. It incorporates bidirectional reflectance distribution functions to account for surface reflectance anisotropy and includes adjacency effects, thus closely mirroring real-world environmental conditions. In accordance with the T-18 system, the irradiance is a sum of contributions from target reflection, scattered sky flux, SIF,

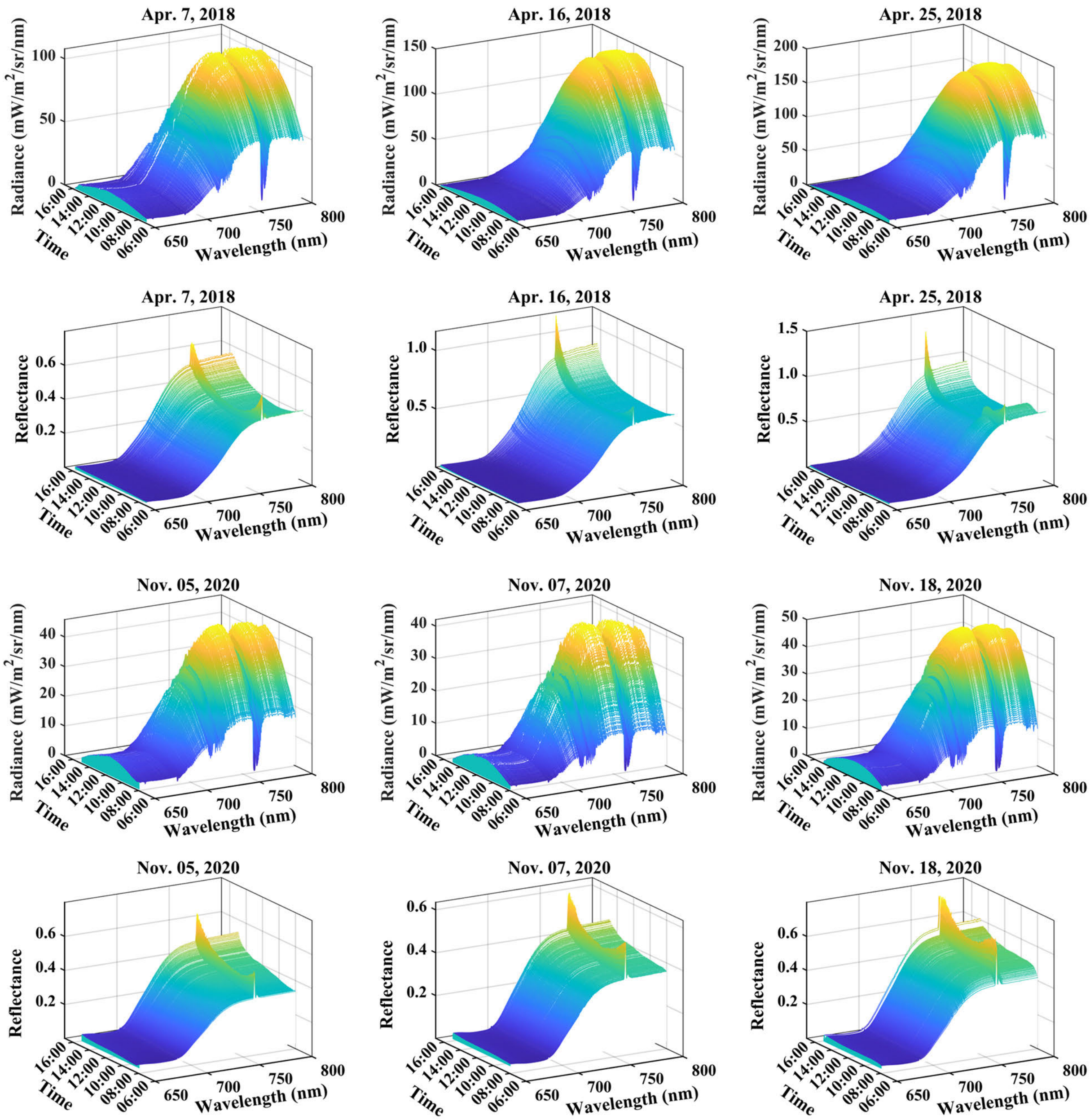


Fig. 1. Provided data represent field-measured canopy upwelling radiance and apparent reflectance, with the upper two rows originating from the Italian site and the lower two rows from the German site.

and adjacency effects. Here, excluding the thermal component, the irradiance $E$ in the observation direction is formulated as

$$E = E_t \cos\theta \tau_{ss} r_{so} + \frac{E_t \cos\theta (\tau_{sd} + \tau_{ss}\overline{r_{sd}}\rho_{dd}) r_{do} + \pi \rho_{dd} \overline{F_d} r_{do}}{1 - \overline{r_{dd}}\rho_{dd}} + \pi F. \quad (1)$$

The corresponding radiance can be calculated by dividing this formula by $\pi$. This procedure involves four reflectance factors, two fluorescence-related factors, and three atmospheric parameters, as detailed in Nomenclature section. The variables $E_t$, $\tau_{ss}$, $\tau_{sd}$, and $\rho_{dd}$ can be derived from the MODTRAN interrogation technique outlined in [36]. The parameters $F$, $F_d$ $r_{so}$, $r_{sd}$, $r_{dd}$, and $r_{do}$ correspond to the outcomes of the SCOPE model. It is important to note that atmospheric variables, such as $\tau_{ss}$, $\tau_{sd}$, and $\rho_{dd}$, are significantly influenced by the absorption of various gases and exhibit substantial correlation across many absorption bands. Consequently, the average value of transmittance product over a finite spectral interval may not be equivalent to the product of the average transmittance. This phenomenon, known as the finite spectral band effect, can be addressed through the computation of the atmospheric transfer functions. Specifically, this involves initially multiplying the parameters according to (1) at the MODTRAN SR (1 cm$^{-1}$) and subsequently convoluting them to the desired SR (0.3 nm in this study), as demonstrated by Cogliati et al. [26] and Verhoef et al. [37]. Instrumental noise

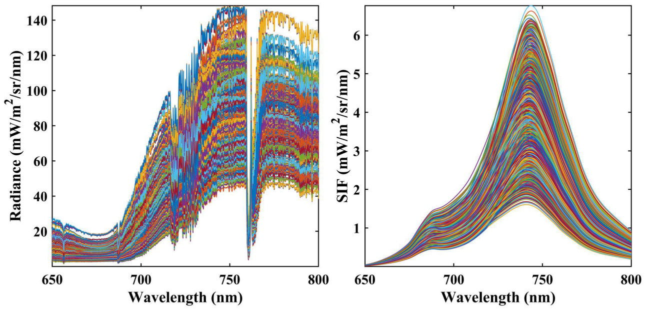


Fig. 2. Canopy upwelling radiance and full-spectrum SIF simulated under 15 atmospheric cases and 288 SCOPE cases.

was added to the simulated upwelling radiance ($L$) based on the following equation [38]:

$$L_{\text{noise}}(\lambda) = L(\lambda) + \left(\text{noise} \cdot \frac{L(\lambda)}{\text{SNR}(\lambda)}\right) \tag{2}$$

where $L_{\text{noise}}$ represents the radiance after the addition of noise, noise is random and follows the standard normal distribution, and $\lambda$ denotes the wavelength. SNR is a function that varies depending on wavelength and radiance and can be expressed as per the formulation proposed by [39]

$$\text{SNR}(\lambda) = \text{SNR}_{\text{ref}} \cdot \sqrt{\frac{L(\lambda)}{L_{\text{ref}}}} \tag{3}$$

where $\text{SNR}_{\text{ref}}$ denotes the reference SNR at the reference radiance level of $L_{\text{ref}}$ and $L_{\text{ref}}$ represents the averaged radiance from 757 to 758 nm.

Two distinct sets of simulations were produced for the purposes of algorithm training and testing. The training dataset comprises a compilation of 15 atmospheric conditions and 5400 SCOPE scenarios, resulting in a comprehensive collection of 81 000 instances. Meanwhile, the testing dataset includes 288 SCOPE scenarios, yielding a total of 4320 instances, collectively referred to as Dataset I. These 15 atmospheric conditions, as described by Verhoef et al. [29], encompass variations in atmospheric parameters such as surface height, humidity, visibility, aerosol type, solar zenith angle (SZA), and atmospheric profile. Table I provides a summary of the atmospheric conditions and the corresponding parameter settings utilized within the SCOPE model. In addition, Fig. 2 displays the simulations used for testing, showcasing the canopy upwelling radiance and full-spectrum SIF across all 4320 scenarios.

SR and SNR constitute fundamental metrics for evaluating sensor performance, particularly within the dominion of SIF retrieval. To systematically investigate the sensitivity of the FSM to variations in SR and SNR, Dataset I was further refined to create datasets with varying levels of SNR and SR. The instrumental spectral response function, crucial for convolution, is modeled as a trapezoidal shape, following the methodology detailed in the referenced study [29]. The SR in these processed datasets spans from 0.1 to 1.0 nm in increments of 0.1 nm, whereas the SNR varies from 100 to 1500 with intervals of 200. This comprehensive approach resulted in the formation of 80 distinct subdatasets, collectively referred to as Dataset II.

## III. Retrieval Methodology

### A. Fourier Series-Based Method

If both reflectance and SIF conform to Lambert's law, the upwelling radiance $L$ at the top of canopy (TOC) over a vegetation target can be approximated as [40]

$$L(\lambda) = \frac{E(\lambda)}{\pi} R(\lambda) + F(\lambda) \tag{4}$$

where $E$ represents the downwelling radiance and $R$ denotes the reflectance devoid of any emission component. Theoretically, all nonconstant parameters in this equation can be considered as functions that fluctuate with wavelength. Due to atmospheric absorption effects, $L$ and $E$ exhibit more pronounced oscillating components, making their functionalized description more challenging, especially in cases of finer SR. On the other hand, $R$ and $F$ exhibit smoother spectral profiles without sharp oscillations, thereby simplifying their modeling efforts. Referring to prior studies [27], [29], the $F$ component can be effectively reconstructed by employing a small number of singular vectors (SVs) derived from the full-spectrum SIF training dataset through the application of the singular value decomposition (SVD) technique [7]. This process captures the essential features of $F$ with considerable efficiency and accuracy. For modeling $R$, we introduce the use of Fourier series, a mathematical tool that decomposes a periodic signal into an infinite series of sines and cosines. These functions, owing to their orthogonal properties, allow for an increasingly precise approximation of the original signal through the summation of higher order or potentially infinite series expansions. In the proposed method, it is assumed that $R$ forms a complete periodicity within the retrieval window, enabling the reflectance spectrum to be approximated to an arbitrary degree of accuracy by summing successive higher order expansions of the Fourier series. Consequently, the aforementioned equation can be reformulated as follows:

$$\begin{aligned} L(\lambda) = \frac{E(\lambda)}{\pi}\Bigg[a_0 + \sum_{i=1}^{n}\Bigg(a_i \cos\left(i\frac{2\pi}{T}(\lambda)\right) \\ + b_i \sin\left(i\frac{2\pi}{T}(\lambda)\right)\Bigg)\Bigg] \\ + \sum_{j=1}^{n_f} \omega_j \psi_j(\lambda) \end{aligned} \tag{5}$$

where $a$ (including $a_0$) and $b$ denote the Fourier coefficients that need to be determined to accurately model the behavior of reflectance, $n$ represents the order of expansion for the Fourier series, $T$ signifies the spectral period and is defined by the span between the two boundary wavelengths within the spectral retrieval window, $n_f$ signifies the number of SIF SVs utilized in the model, and $\omega_j$ represents the weight coefficient of SV $\psi_j$.

Determining the appropriate order for the Fourier series plays a crucial role in the framework of the FSM, as the essence of this method lies in reconstructing reflectance

TABLE I
ATMOSPHERIC SCENARIOS AND SCOPE PARAMETERS SETTINGS FOR SIMULATED DATA

| Parameters of SCOPE | Value | | Unit | Description |
|---|---|---|---|---|
| | Training | Test | | |
| *Cab* | 5, 10, 30, 50, 70 | 20, 40, 60 | μg/cm$^2$ | Chlorophyll a+b content |
| *Cdm* | 0.01, 0.02, 0.03 | 0.015, 0.025 | g/cm$^2$ | Dry matter content |
| *Cw* | 0.01, 0.03 | 0.02 | cm | Leaf water equivalent layer |
| *N* | 1.0, 2.0, 3.0 | 1.5, 2.5 | - | Leaf thickness parameters |
| *fqe* | 0.01, 0.02 | 0.015, 0.025 | - | Fluorescence quantum yield efficiency |
| *LAI* | 1, 3, 5 | 2, 4 | - | Leaf area index |
| *LIDFa* | −0.35, 0 | −0.35, 0 | - | Leaf Inclination Distribution Function (LIDF) parameter a |
| *LIDFb* | −0.15, 0 | −0.15, 0 | - | LIDF parameter b |
| Atmospheric cases | Standard | Variations | Unit | Description |
| *H₂* | 0.4 | 0/1.2 | km | Surface height |
| *Visibility* | 20 | 5/10/40/80 | km | Surface meteorological range |
| *Humidity* | 1× | 0.5×/1.5× | times to default | Vertical water vapor column |
| *IHAZE* | rural | Maritime/ urban | - | Aerosol type |
| *MODEL* | 2 | 1/3 | - | Atmospheric profile |
| *SZA* | 45 | 30/60 | Degree | solar zenith angle |

through Fourier series expansions. Within the presented retrieval framework, full-spectrum SIF retrieval can be achieved by setting a higher order expansion of the Fourier series. However, it is essential to recognize the tradeoffs involved in setting a higher $n$. Increasing $n$ escalates the number of parameters to be estimated within the model, leading to diminished computational efficiency and requiring more computational time. In addition, as $n$ increases, similar periodic variations occur between spectra produced by different Fourier series expansions. Fig. 3 illustrates the variation of average relative root-mean-square error (RRMSE) and $R^2$ corresponding to the results of reconstructing the reflectance in Dataset I using different orders of Fourier series. The accuracy of the reflectance reconstruction results gradually improves as the number of orders increases. Moreover, the RRMSE values descend more slowly at orders higher than 150, primarily due to the variability in reflectance interpretation decreasing with increasing order. During this process, $R^2$ does not change significantly as it consistently remains at a high value. Eventually, at an order of 350, the average RRMSE value is below 0.1%, while $R^2$ is nearly 1.

The correlation between spectra due to similar periodicity of higher order expansions can be mitigated by spectral downscaling, a process that simplifies the spectra while preserving the essential features. To streamline the model and enhance computational efficiency, we adopted the SVD technique for feature extraction from the spectral matrix that encompasses spectra from the leading 350 orders of the Fourier series expansions. Correspondingly, the Fourier series expansions of different orders can be obtained by using [1 $\cos\left(1\frac{2\pi}{T}(\lambda)\right) + \sin\left(1\frac{2\pi}{T}(\lambda)\right) \cos\left(2\frac{2\pi}{(T}(\lambda)\right) + \sin\left(2\frac{2\pi}{T}(\lambda)\right) \cdots \cos\left(n\frac{2\pi}{(T}(\lambda)\right) + \sin\left(n\frac{2\pi}{T}(\lambda)\right)$], which is the Fourier series without fitting coefficients. Then, a number of Fourier series SVs ($\varphi$) were

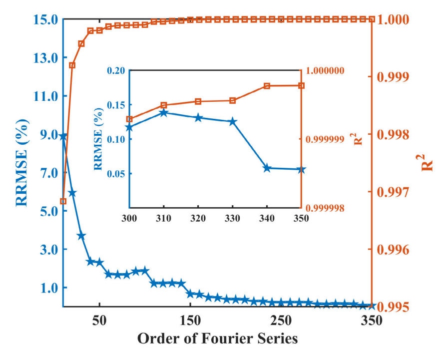


Fig. 3. Effect of using different numbers of Fourier series on the RRMSE and $R^2$ of the reflectance reconstruction results in Dataset I.

utilized to represent the reflectance item, thus streamlining the model. Consequently, the final retrieval model can be articulated as

$$L(\lambda) = \frac{E(\lambda)}{\pi} \sum_{i=1}^{n_{fs}} \alpha_i \varphi_i(\lambda) + \sum_{j=1}^{n_f} \omega_j \psi_j(\lambda) \tag{6}$$

where $\alpha_i$ represents the weight coefficient of $\varphi_i$ and $n_{fs}$ indicates the number of Fourier series SVs employed in the retrieval model. In this model, the state vector elements are $\alpha$ and $\omega$, whereas $\varphi$ and $\psi$ serve as the model parameters. This equation can be solved by ordinary least-squares fitting.

Fig. 4 showcases the leading 27 Fourier series SVs. These SVs cumulatively account for over 99.99% of the total variance in the information. Notably, from the 13th SV onward, a consistent periodicity is observed across the Fourier series SVs. This periodicity can be closely approximated by sine and cosine functions with varying degrees of offsets along the $x$-axis. Leveraging different weighting coefficients allows for

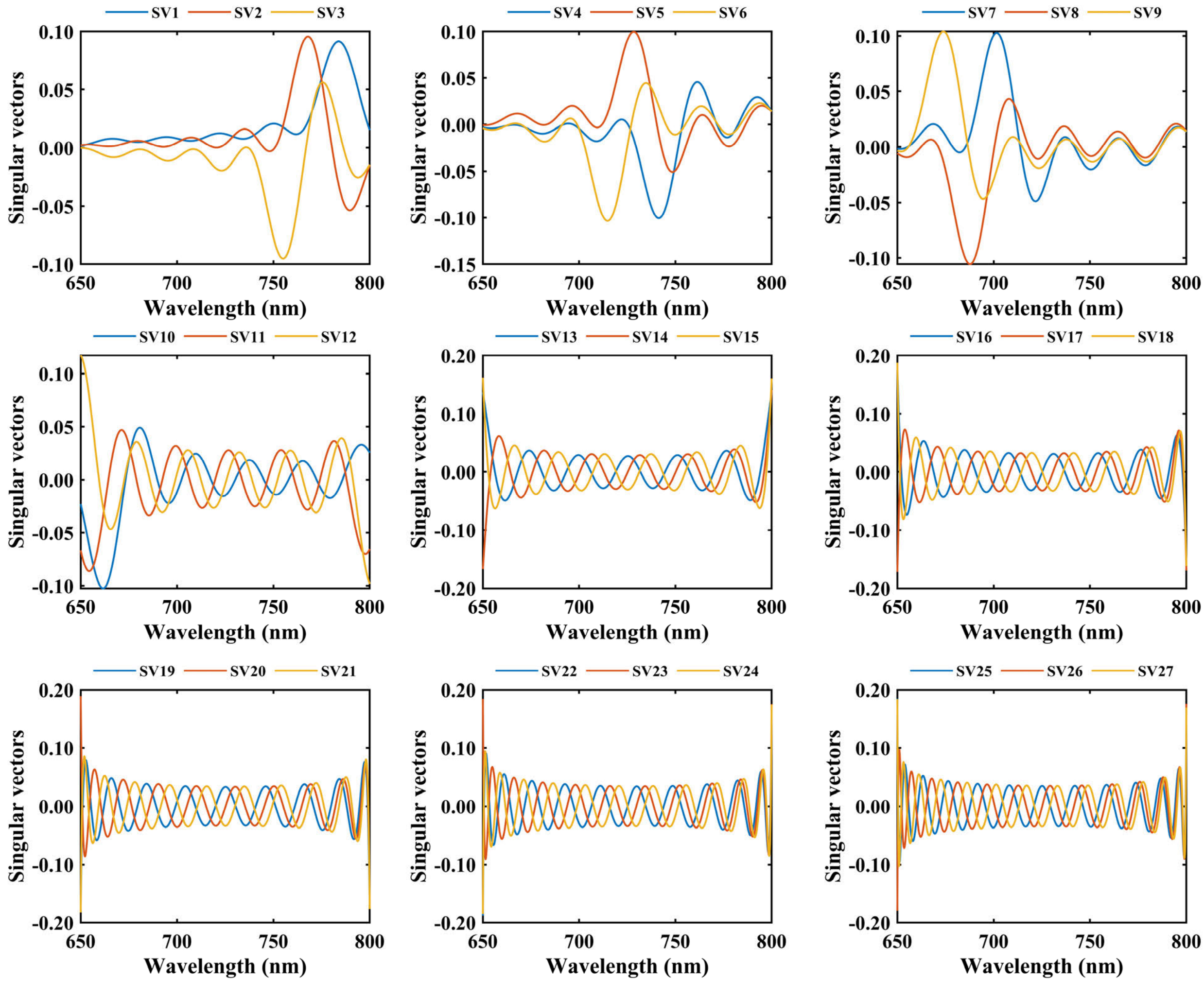


Fig. 4. First 27 SVs extracted from the spectral library consisting of the leading 350th order Fourier series expansions.

precise reconstruction of reflectance based on these periodic signals. Regarding the SIF SVs, the spectral shapes and features exhibit similarities to those presented by Zhao et al. [27].

It is noteworthy that (6) aligns with the final model of the aFSR method as presented by Zhao et al. [27]. However, a fundamental difference lies in the interpretation of reflectance reconstruction between these two models. The aFSR method relies on reflectance SVs (or basis spectra) obtained through feature extraction from a dedicated reflectance training dataset. This process inherently ties the model's effectiveness to the representativity of the available training data. Conversely, (6) employs Fourier series SVs derived from the Fourier series expansions, which remain consistent irrespective of changes in the training datasets. This significant distinction enables the FSM to operate independently of a specific reflectance training dataset, presenting a substantial advantage in terms of applicability and flexibility.

In practical scenarios, the representativeness of the training dataset for a given vegetation reflectance is crucial in the aFSR method. Insufficient representation of similar reflectance scenarios in the training dataset could potentially compromise the accuracy of the retrieval process. In contrast, the FSM method overcomes this limitation by utilizing the inherent property of Fourier series to successively approximate the original signal. This means that irrespective of the variability in vegetation reflectance, the FSM can theoretically reconstruct the reflectance profile accurately by optimizing the weighting coefficients for the Fourier series SVs. This capacity to adapt to various reflectance scenarios without the need for a comprehensive, scenario-specific training dataset marks a significant advancement over traditional methods, enhancing the FSM's applicability across a broader range of vegetation types and conditions. Fig. 5 illustrates the flowchart of the FSM.

### *B. Accuracy Assessment*

In this study, the following metrics are employed to evaluate retrieval accuracy: the coefficient of determination ($R^2$), RMSE, and RRMSE. The RRMSE is mainly used to evaluate the retrieval accuracy for simulated data, while $R^2$ and RMSE are used for all test data. These metrics are calculated as follows: (7)–(9), as shown at the bottom of the next page, where $\mathrm{SIF}_{\mathrm{ret},i}(\lambda)$ and $\mathrm{SIF}_{t,i}(\lambda)$ are the retrieved SIF and the true or reference SIF at wavelength $\lambda$, respectively; $\overline{\mathrm{SIF}_{\mathrm{ret}}}$ and $\overline{\mathrm{SIF}_t}$ are the average values of all retrieved and true or reference SIF, respectively; and $n$ refers to the total SIF values involved in the calculation.

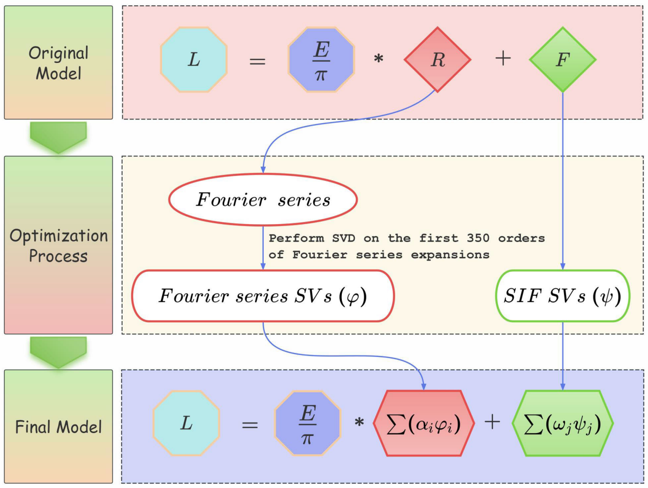


Fig. 5. Flowchart of the FSM algorithm.

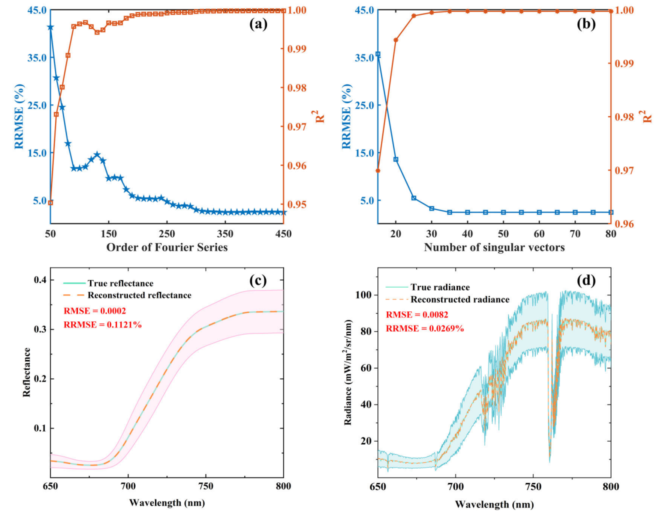


Fig. 6. (a) Retrieval accuracy varies with the order of expansion of the Fourier series. (b) Retrieval accuracy varies with the number of SVs. (c) Reconstruction results for reflectance, where the shaded area represents the standard deviation of the reflectance. (d) Reconstruction results for radiance, where the shaded area represents the standard deviation of the radiance. True refers to simulated data.

## IV. Results

### A. Parameterization of SIF Retrieval Methods

To determine an appropriate the Fourier series expansion order for the FSM, a systematic experiment utilizing Dataset I was carried out. The orders were methodically varied from 50 to 450, in increments of 10, as defined by (5), while employing the first three SIF SVs. Fig. 6(a) illustrates the relationship between the order of Fourier series expansions and the retrieval accuracy, as evidenced by the average RRMSE and $R^2$ across various orders. Notably, as the order increases, a decreasing trend in RRMSE and an increasing trend in $R^2$ can be observed, indicating that accuracy improves with higher orders of the Fourier series. This trend continues until it reaches a plateau, suggesting that beyond a certain order, additional increases do not significantly enhance the retrieval accuracy. This leads to a final order selection of 350.

To enhance retrieval efficiency and mitigate the computational burden associated with higher order Fourier series expansions, Fourier series SVs were employed to approximate reflectance according to (6). Fig. 6(b) illustrates the retrieval accuracy achieved with varying numbers of Fourier series SVs. Consistent with earlier observations, retrieval accuracy initially improves, stabilizing with an increased number of SVs. Ultimately, the determination of 40 SVs proved sufficient. These established settings were then applied to (6). Fig. 6(c) and (d) depicts the results of reflectance and radiance reconstruction based on the test data. Both figures reveal remarkably high reconstruction accuracies, with RMSE values of 0.0002 and 0.0082 mW/m$^2$/sr/nm, and RRMSE values of 0.1121% and 0.0269%, respectively.

The retrieval setup for the SFM in the oxygen bands was guided by insights from previous literature [24]. In addition, second-order Taylor polynomials were employed to characterize the variation of reflectance and fluorescence within the retrieval window. For the aFSR method, the parameterization strategy involved utilizing the leading 20 reflectance SVs and the first three SIF SVs. This strategy was adopted due to occasional inadequacies observed when applying the Bayesian information criterion to field data. The selection of the leading 20 reflectance SVs was motivated by their proven efficiency in achieving robust retrievals. Similarly, within the FSM, the adoption of the first three SIF SVs ensures the retrieval of comprehensive full-spectrum SIF details. This decision is particularly important because only the first two SIF SVs for full-spectrum SIF retrieval in either the FSM or aFSR methods lead to an underestimation of the red SIF. Conversely, employing the first four SIF SVs introduces a spectral anomaly in the SIF retrieval, potentially attributed to overfitting. Table II

$$R^2 = \left(\frac{\sum_{i=1}^{n}\left(\mathrm{SIF}_{\mathrm{ret},i}(\lambda) - \overline{\mathrm{SIF}_{\mathrm{ret}}}\right)\cdot\left(\mathrm{SIF}_{t,i}(\lambda) - \overline{\mathrm{SIF}_{t}}\right)}{\sqrt{\sum_{i=1}^{n}\left(\mathrm{SIF}_{\mathrm{ret},i}(\lambda) - \overline{\mathrm{SIF}_{\mathrm{ret}}}\right)^2}\cdot\sqrt{\sum_{i=1}^{n}\left(\mathrm{SIF}_{t,i}(\lambda) - \overline{\mathrm{SIF}_{t}}\right)^2}}\right)^2 \tag{7}$$

$$\mathrm{RMSE} = \sqrt{\frac{\sum_{i=1}^{n}\left(\mathrm{SIF}_{\mathrm{ret},i}(\lambda) - \mathrm{SIF}_{t,i}(\lambda)\right)^2}{n}} \tag{8}$$

$$\mathrm{RRMSE} = \sqrt{\frac{\sum_{i=1}^{n}\left(\frac{\mathrm{SIF}_{\mathrm{ret},i}(\lambda)-\mathrm{SIF}_{t,i}(\lambda)}{\mathrm{SIF}_{t,i}(\lambda)}\right)^2}{n}} \times 100\% \tag{9}$$

TABLE II
PARAMETER SETTINGS FOR ALL RETRIEVAL METHODS

| Method | Retrieval window (nm) | Number of SVs representing reflectance | Number of SVs representing SIF |
|---|---|---|---|
| FSM | 650–800 | 40 | 3 |
| aFSR | 650–800 | 20 | 3 |
| SFM | 684–692/ 757–771 | - | - |
| SpecFit | 670–780 | - | - |

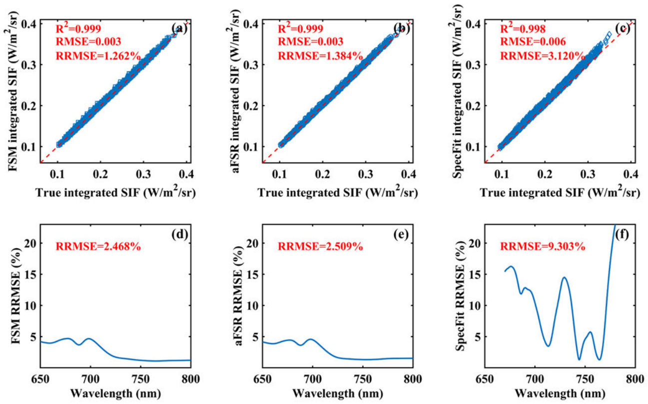


Fig. 7. Scatter plot of the spectrally integrated true SIF spectra versus (a) FSM-retrieved, (b) aFSR-retrieved, and (c) SpecFit-retrieved. RRMSE varies with wavelength for (d) FSM, (e) aFSR, and (f) SpecFit methods.

summarizes the parameter configurations employed in all SIF retrieval methods within the scope of this study.

### B. Results for Synthetic Data

Fig. 7(a) and (b) presents the comparison of spectrally integrated SIF of the FSM and aFSR methods within the spectral range of 650–800 nm, while Fig. 7(c) shows the results for the SpecFit method in the range of 670–780 nm. Both the FSM and aFSR methods exhibited retrieval results closely aligned with the true SIF, as evidenced by RMSE values of 0.003 W/m$^2$/sr and RRMSE values of 1.262% for FSM and 1.384% for aFSR, respectively. In contrast, the SpecFit method showed relatively lower accuracy in full-spectrum SIF retrieval, with an RRMSE value of 3.12%, which is more than twice that of the FSM and aFSR methods.

Fig. 7(d)–(f) illustrates the variation of retrieval RRMSE with wavelength for the three methods. A comparable distribution can be observed between the FSM and aFSR methods, indicating a gradual decrease in RRMSE from the red to the near-infrared range. This might be attributed to the spectral complex inherent in the red SIF range, which requires an accurate reconstruction of the first SIF peak and SIF valley. The SpecFit method exhibited noticeably higher and more heterogeneous distribution of RRMSE values compared to the FSM and aFSR methods, with an average RRMSE of 9.303%, significantly higher than 2.468% and 2.509% observed for the FSM and aFSR methods, respectively.

Fig. 8 shows the results of single-band SIF retrieval across the $O_2$-A and $O_2$-B bands, as performed by the FSM, aFSR, SpecFit, and SFM methods. In the $O_2$-B band, the FSM, aFSR, and SFM methods demonstrate comparable retrieval accuracies, with slight variations across different metrics and all RRMSE values remaining below 3.73%. The SpecFit method, however, exhibits a lower retrieval accuracy with an RRMSE of 12.043%. Similar conclusions can be drawn from the results of the $O_2$-A band. Specifically, RRMSE values for the $O_2$-A band are significantly reduced, being at least half the magnitude of those observed in the $O_2$-B band. For the SFM method, the improved accuracy in the $O_2$-A band may be attributed to its increased sensitivity to atmospheric absorption. The deeper absorption line within this band enables more precise SIF retrieval. In contrast, for the other three methods, the simpler SIF reconstruction in the near-infrared range relative to the red band may account for the observed results.

Dataset II was utilized to investigate the sensitivity of the FSM method with regard to SR and SNR. Fig. 9 presents contour plots illustrating how the accuracy of full-spectrum SIF retrieval varies with changes in SR and SNR for the FSM method. It is noteworthy that finer SR values, for a constant SNR, are associated with enhanced retrieval accuracy. Similarly, an increase in SNR contributes to improved accuracy while keeping SR constant. The optimal retrieval accuracy for the FSM method is attained at an SR of 0.1 nm and an SNR of 1500, resulting in an average RRMSE value of 1.815%. Most combinations of SR and SNR (located in the top-left regions of the plots) correspond to lower RRMSE values, for instance, less than 15%. Conversely, the bottom-right regions indicate a steep decline in retrieval accuracy due to higher SR and lower SNR settings.

### C. Results for Field Data

Fig. 10 depicts the diurnal full-spectrum SIF retrievals for the FSM, aFSR, and SpecFit methods across various dates at the Italian site. The retrieval results of all three methods exhibit satisfactory agreement, effectively reconstructing the double-peak feature of full-spectrum SIF with well-defined valleys. The observed diurnal trend of the retrieval results, characterized by an increase in the morning followed by a decrease in the afternoon, aligns consistently with findings from prior studies. Moreover, there is a discernible upward trend in retrieval results as the date progresses. An anomaly is noted in the full-spectrum SIF retrievals of the aFSR method on April 25, where negative values are observed around 710 nm, dipping to approximately $-0.5$ mW/m$^2$/sr/nm. Such occurrence contradicts the expected characteristics of the SIF spectrum and indicates retrieval uncertainty specific to the aFSR method. In contrast, retrievals performed using the FSM do not exhibit this phenomenon, underscoring its stability and robustness in practical applications. Furthermore, the SpecFit method, constrained to a limited range of SIF spectra (from 670 to 780 nm), shows less pronounced valleys compared to the FSM approach, which comprehensively captures the entire full-spectrum SIF range.

Fig. 11 illustrates the diurnal results of the full-spectrum SIF retrieved by the three methods across different dates at the German site. The diurnal trend observed in the full-spectrum

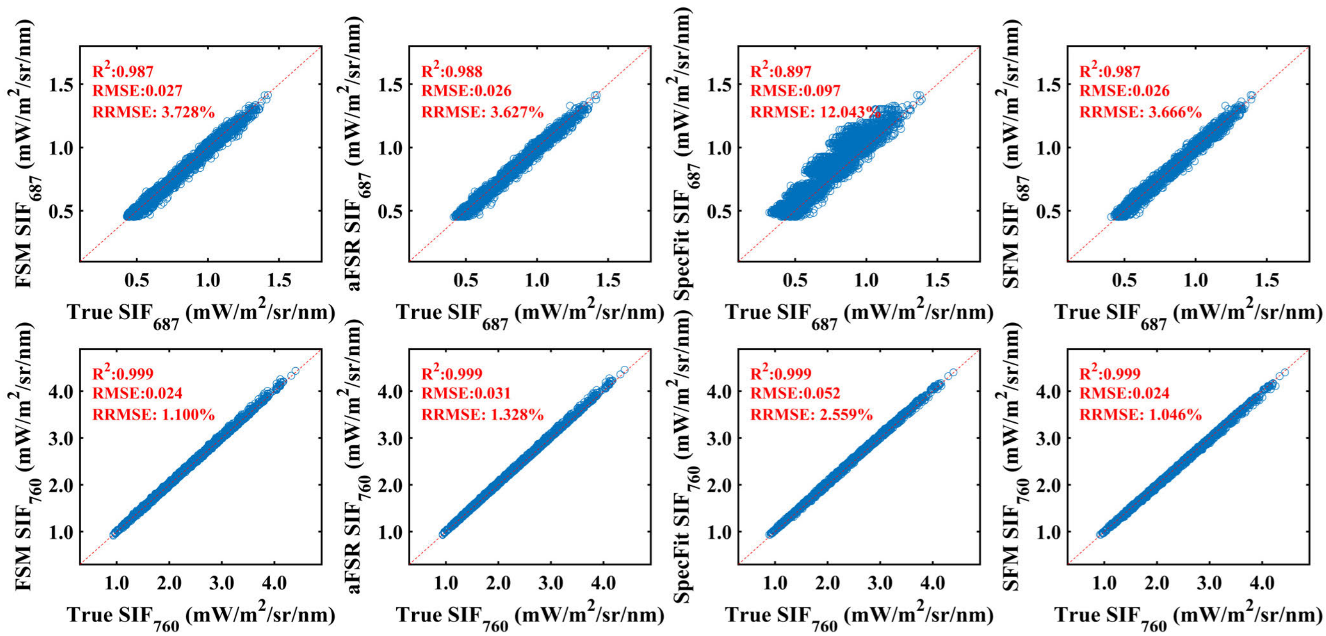


Fig. 8. Top row gives the scatter plots of the true SIF at 687 nm versus the SIF values retrieved through the employment of the FSM, aFSR, SpecFit, and SFM methods. The bottom row shows the comparison of the retrieval results at 760 nm for the four methods.

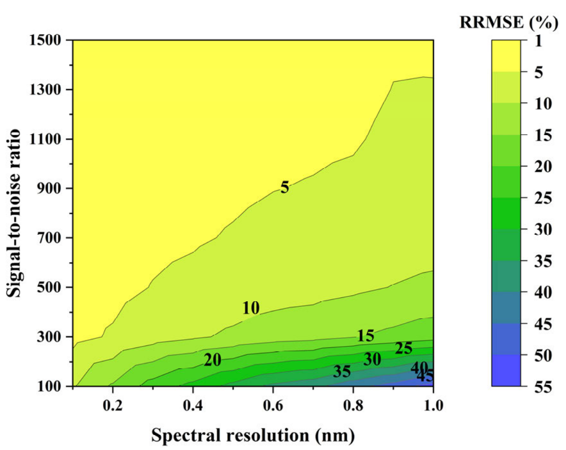


Fig. 9. Contour plots of the average RRMSE values of the full-spectrum SIF retrieved by the FSM as a function of SR and SNR.

SIF data corresponds closely to findings noted at the Italian site, indicating consistency in the temporal dynamics of SIF emissions between the two locations. Both the FSM and aFSR methods exhibit highly consistent retrieval results, characterized by similar spectral shapes and magnitudes across the measured dates. In contrast, while the SpecFit method yields comparable magnitudes of full-spectrum SIF, the spectral shapes notably differ. Specifically, the SpecFit results show distinct double-peak features that are less apparent in the FSM and aFSR method results. Indeed, the sparse coverage of the observed targets at the German site corresponds to a relatively low chlorophyll content, which attenuates the reabsorption effect of fluorescence. It is thus more likely that the FSM and aFSR methods captured accurate SIF spectral features.

Fig. 12 presents a comparison between the average apparent reflectance collected on six dates and the average reflectance reconstructed by the FSM, aFSR, and SpecFit methods. The top row illustrates the average reflectance at the Italian site, which showcases greater variability among the dates and an observable increasing trend over time. In contrast, the bottom row depicts the average reflectance at the German site, displaying a more moderate increasing trend.

In Fig. 12, the comparison of reflectance reconstruction between the FSM, aFSR, and SpecFit methods reveals a high level of agreement in the overall value domains, indicating a general consistency in the full-spectrum SIF retrieved by these methods. However, differences in detail within the local spectral range are evident. For instance, the reflectance reconstructed by the aFSR method in the $O_2$-B band on April 25, 2018, is notably higher than those of the FSM and SpecFit methods, indicating potentially lower SIF values retrieved by the aFSR method. In addition, a significant downward anomalous vibration is observed for all $O_2$-A band reflectance reconstructions at the Italian site using the aFSR method, implying potentially anomalous and higher SIF values compared to the FSM and SpecFit retrievals. For the German site, corresponding to the bottom row in Fig. 12, the magnitude of the anomalous vibration in the $O_2$-A band is significantly reduced for the aFSR method. The reflectance reconstruction results of the SpecFit method are in good agreement with those of the FSM and aFSR methods in most of the spectral region but are slightly lower at both ends, suggesting that the SIF values are higher than those of the previous two methods in the corresponding bands.

The reliability of full-spectrum SIF retrieved from canopy measurements is further validated through single-band SIF retrievals. The diurnal variations of single-band SIF at the $O_2$-A and $O_2$-B bands retrieved by the SFM, FSM, aFSR, and SpecFit methods are illustrated in Fig. 13. Results for different bands at the same site are indicated by the identically

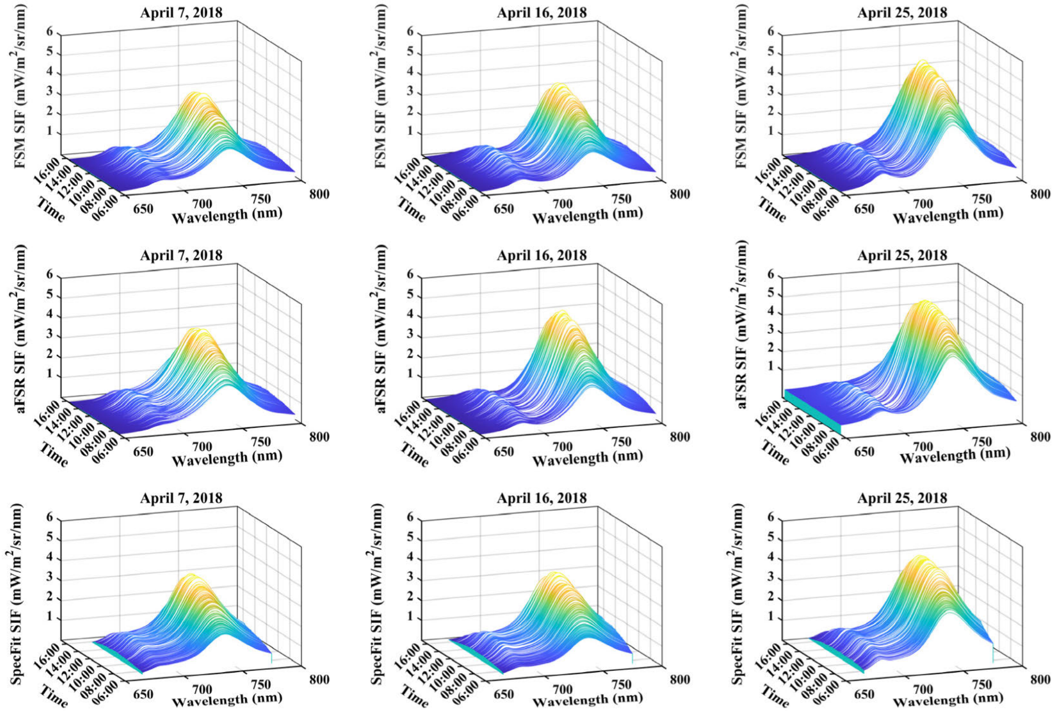


Fig. 10. Diurnal variation of the full-spectrum SIF retrieved by the FSM, aFSR, and SpecFit methods for measurements conducted on various dates at the Italian site.

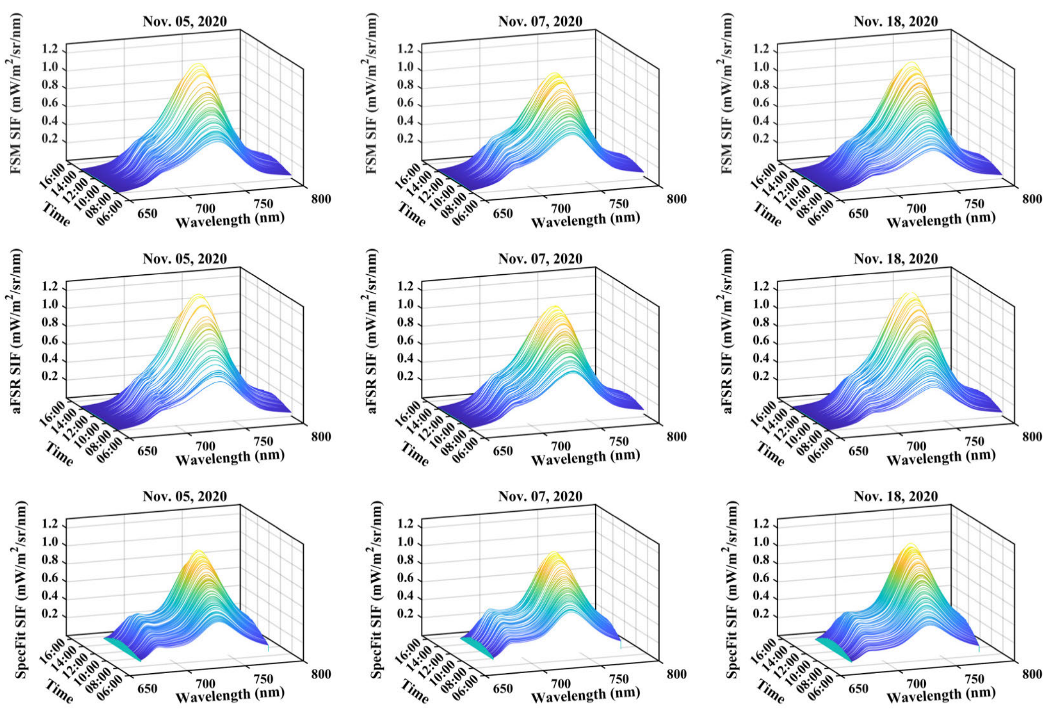


Fig. 11. Diurnal variation of the full-spectrum SIF retrieved by the FSM, aFSR, and SpecFit methods for measurements conducted on various dates at the German site.

colored bars. For the Italian site in the left column, a noticeable gradual increase in the retrieved SIF is observed in both bands as the growing season progresses. In the $O_2$-B band, SIF retrievals on April 7 and 16, 2018, reveal clear consistency across the four methods. However, a noticeable deviation emerges on April 25, where the SIF values retrieved by the aFSR method appear lower than those by the other methods, suggesting potential underestimation. This trend aligns with observations from Fig. 12, which highlighted discrepancies in localized reflectance reconstruction, particularly in the $O_2$-B

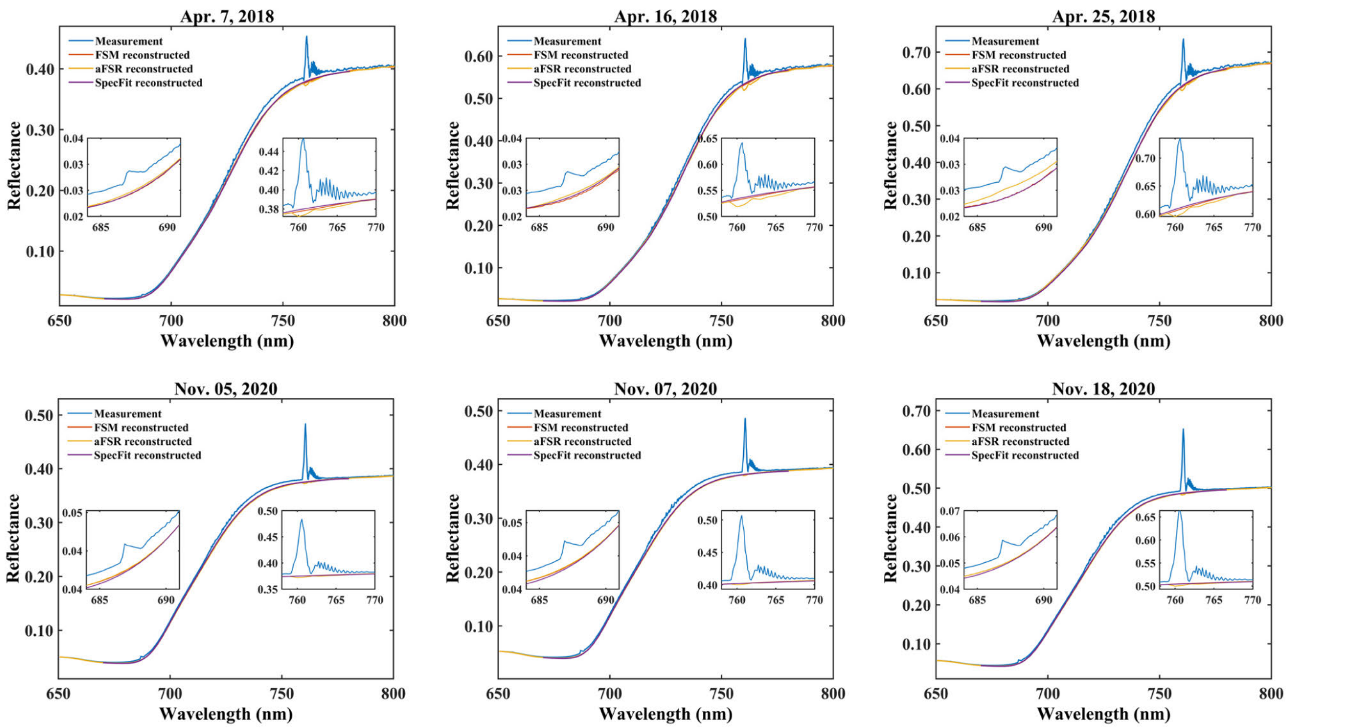


Fig. 12. Top row shows the measured apparent reflectance and the reflectance reconstructed by the FSM, aFSR, and SpecFit methods for April 7, 16, and 25, 2018, at the Italian site. The bottom row depicts the corresponding results for German site on November 5, 7, and 18, 2020. Two additional local magnifications show the reconstruction results of the $O_2$-A and $O_2$-B bands, respectively.

band, where aFSR's reconstructed results were notably higher. On the other hand, the aFSR method consistently reports higher SIF values in the $O_2$-A band, indicating potential overestimation. This observation correlates with the anomalies in reflectance reconstruction for the $O_2$-A band identified in Fig. 12, where aFSR exhibited significant downward anomalous vibrations, suggesting discrepancies in its SIF retrieval process. In contrast, the agreement between the FSM and SFM retrievals stands out across both the $O_2$-A and $O_2$-B bands, indicating a strong alignment in capability to accurately capture SIF. At the German site, shown in the right column, the retrieval results of the SpecFit method at the $O_2$-B band show higher SIF values compared to the other methods. Minimal differences are observed in the $O_2$-A band, but overall, there is a higher degree of agreement between the methods.

Given that the single-band SIF retrieval method, SFM, is a relatively well-established technique and has been considered a reference in many studies [17], [41], [42], this study also employs the SFM method as the reference SIF for $O_2$-A and $O_2$-B bands to assess the reliability of the full-spectrum SIF retrieval methods FSM, aFSR, and SpecFit.

Fig. 14 offers a detailed quantitative analysis of single-band SIF retrieval results. At the Italian site, the FSM and SpecFit methods show better agreement between the single-band retrieval results and the reference SIF, with the FSM yielding $R^2$ values of 0.966 and 0.998 for the $O_2$-B and $O_2$-A bands, respectively, corresponding to RMSE values of 0.069 and 0.118 mW/m$^2$/sr/nm. In contrast, the aFSR method shows slightly poorer results for these two bands, with $R^2$ values of 0.809 and 0.980, and RMSE values of 0.116 and 0.506 mW/m$^2$/sr/nm. This discrepancy is likely due to the

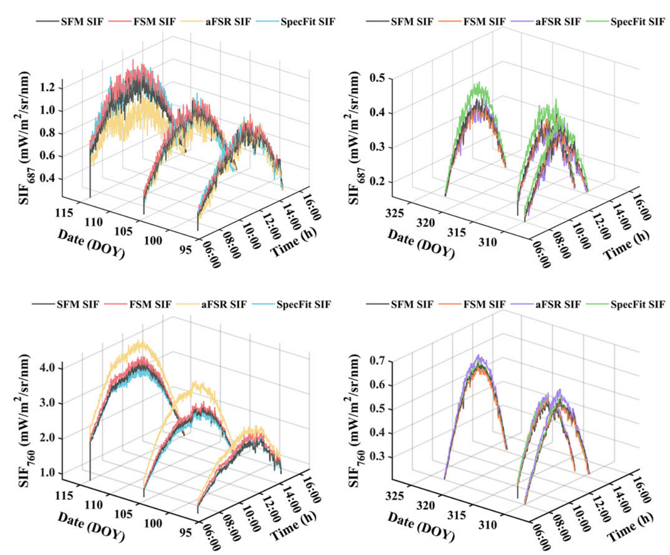


Fig. 13. Left column presents the diurnal SIF retrievals in the oxygen bands on April 7 and 16, 2018, for the Italian site, retrieved by the SFM, FSM, aFSR, and SpecFit methods. The right column provides the corresponding results on November 5, 7, and 18, 2020, for the German site. The top row of retrievals refers to the SIF at 687 nm and the bottom row of results corresponds to the SIF at 760 nm.

aFSR method's under-representation of the reflectance training dataset. For the German site, there is a better alignment between the retrieval results of the three methods and the reference SIF, mostly demonstrated by the improved performance of the aFSR method. The lowest $R^2$ in the $O_2$-B and $O_2$-A bands is 0.969 and 0.988, respectively, and the highest RMSE is only 0.035 mW/m$^2$/sr/nm.

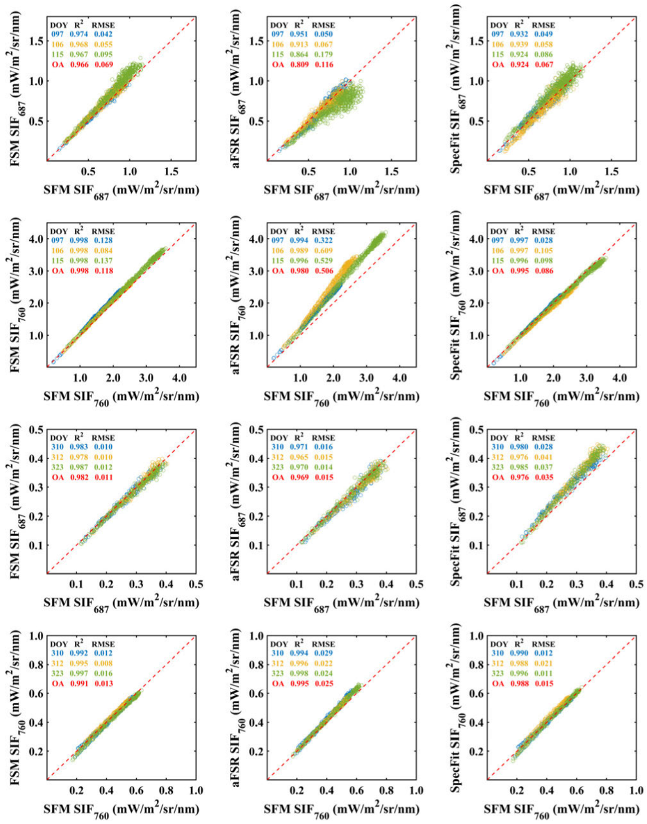


Fig. 14. Scatterplots displayed in the top two rows represent the single-band SIF for the Italian site, while those in the bottom two rows depict the corresponding scatterplots for the German site. Each color in the scatterplot represents the results for different dates. Highlighted in red is the overall accuracy (OA), which signifies that the accuracy metrics are calculated with data from all dates.

It is crucial to acknowledge the inherent challenge in obtaining precise SIF measurements in field conditions introduces a degree of uncertainty in these presented results. Consequently, while these findings offer significant insights into the comparative accuracy and reliability of the FSM, aFSR, and SpecFit methods, they should be interpreted as indicative of potential performance rather than conclusive representations of practical retrieval accuracy.

## V. DISCUSSION

### A. Performance of FSM

Several existing methods for full-spectrum SIF retrieval, such as the FSR [24], F-SFM [25], and aFSR [27], entail specific prerequisites to achieve high-accuracy retrieval. The FSR method relies on the accuracy of single-band SIF retrievals, which are limited to a few oxygens and water vapor bands. The F-SFM and aFSR methods depend on the representativeness of reflectance training dataset, which is used to derive reflectance SVs necessary for spectral reconstruction. Ensuring sufficient representativeness requires the dataset to encompass diverse combinations of canopy parameters, mirroring the multifaceted nature of real-world scenarios, thereby ensuring that the retrieval process can accurately capture the complexity and variability inherent in natural ecosystems. This diversity is crucial for the retrieval process to accurately capture the complexity and variability inherent in natural ecosystems. Inadequate representativeness in the training dataset may lead to compromised accuracy or retrieval errors. Besides, the SpecFit method, proposed by Cogliati et al. [26] and simplified by Cogliati et al. [43], does not rely on a training dataset but can only retrieve SIF spectra within a limited spectral range due to the manifestation form of the SIF spectrum. Similarly, WAFER [41], a wavelet decomposition-based SIF retrieval method, does not introduce coupling between reflectance and fluorescence, aligning with the principle of the proposed FSM. Although the WAFER method can theoretically achieve full-spectrum SIF retrieval, it is currently only used for fixed-range SIF retrieval. Furthermore, the wavelet decomposition performed in each iteration significantly increases the computational cost of the WAFER method.

In this study, the proposed FSM approach conceptualizes reflectance as a wavelength-dependent function while approximating the reflectance through the successive summation of higher order expansions of the Fourier series. This innovative approach adeptly addresses the issue of under-representation encountered in prior methods. Simultaneously, the FSM overcomes the drawbacks of the SpecFit and WAFER methods by achieving complete full-spectrum SIF retrieval and smaller computational cost through the higher order Fourier series expansion and SVD decomposition, which only need to be executed once.

Results based on synthetic data reveal that the FSM approach exhibits robust full-spectrum SIF retrieval capabilities across diverse combinations of atmospheric and canopy parameters, yielding average RRMSE values of 2.468%, which is lower than that of the aFSR method (2.509%) and the SpecFit method (9.303%). Moreover, the spectral integration of the full-spectrum SIF further highlights the excellent accuracies achieved by the FSM, with an RRMSE value of 1.262%, which is also lower than that of the aFSR method (1.384%) and the SpecFit method (3.120%). Sensitivity analyses showed the response of the FSM approach to different combinations of SRs and SNRs, with practical implications for sensor manufacturing. Purposeful adjustments in SNR simplify the sensor production process while adhering to requirements for full-spectrum SIF retrieval. As illustrated in Fig. 9, sensors designed with an SR of 0.1 nm and an SNR surpassing 300 are capable of achieving RRMSE values below the 5% threshold. Conversely, sensors featuring lower SR values benefit from augmented SNR to enhance retrieval accuracy. For instance, maintaining an RRMSE below 5% is feasible with an SR of 0.8 nm and an SNR of 1100. It is essential to emphasize that the utilization of simulated data, although idealized and subject to less uncertainty compared to field measurements, serves as a valuable tool in demonstrating the theoretical viability and performance of the FSM approach.

In the reflectance reconstruction based on field measurements, the comparative analysis reveals that the FSM, aFSR, and SpecFit methods yield similar results, albeit with nuanced differences. Notably, the FSM-based reconstruction aligns more closely with empirical observations, particularly in its rendition of reflectance across the $O_2$-A band. This contrast is marked by a smoother reflectance curve achieved through the FSM, as opposed to the aFSR method, which is characterized by pronounced anomalous fluctuations in the same spectral region. Given that SIF contributes only a fraction to the apparent reflectance, even minor deviations in reflectance reconstruction can result in considerable variations in retrieved SIF values. For instance, an example on April 25, 2018, at the Italian site revealed that the reflectance results obtained through the aFSR method in the $O_2$-B band were anomalously high. This aberration led to a noticeable underestimation of the SIF values when compared to reference SIF. Conversely, at the same Italian site, the diminished reflectance reconstruction in the $O_2$-A band for the aFSR method resulted in significantly higher SIF relative to the reference data, as delineated in Figs. 12 and 13. This discrepancy can be attributed to the lack of representativeness of the reflectance training dataset utilized in the aFSR method, consequently leading to retrieval errors. The Italian site exhibited high average values of apparent reflectance, which were not adequately represented in the training dataset, thereby contributing to its under-representation. In comparison, the apparent reflectance measured at the German site was relatively low and routine, with similar reflectance patterns included in the training dataset, thereby yielding aFSR-retrieved SIF values closer to those obtained through other methods.

In the comparative analysis of the diurnal variation in single-band SIF, notable discrepancies are observed, particularly with the retrieval outcomes of the aFSR method at the Italian site. These discrepancies are evidenced by a significantly elevated RMSE value of 0.506 mW/m$^2$/sr/nm in the $O_2$-A band and a markedly lower $R^2$ value 0.809 in the $O_2$-B band, indicative of deviations between its results and the reference SIF. Conversely, the FSM demonstrates superior outcomes, evidenced by a significantly reduced RMSE value of 0.118 mW/m$^2$/sr/nm and an enhanced $R^2$ value of 0.966 when compared with reference SIF. These findings underscore the superior performance of the FSM in accurately capturing diurnal variations of SIF.

Although the FSM shows promise for full-spectrum SIF retrieval, it is imperative to acknowledge its shared limitations. The SIF SVs utilized in FSM are derived from the 1-D model SCOPE, which, albeit informative, lacks the comprehensive representation of the 3-D complexities inherent in natural environments. This limitation arises from the oversimplification of 1-D models, neglecting the more intricate influences of absorption and scattering present in the 3-D real-world scenario. A potential avenue to address this limitation involves integrating SIF training datasets generated from 3-D models, such as the DART [44] and FluorWPS models [45]. Leveraging these datasets holds the promise of providing a more precise and comprehensive depiction of SIF spectra, by incorporating the complexities introduced by the 3-D nature of the environmental conditions. Moreover, it is paramount to validate the reliability of FSM through extensive validation with additional field data collected from various sensors and targets. Expanding the dataset will facilitate a comprehensive assessment of the generalizability and robustness of FSM across diverse environmental conditions and measurement setups. Such validation efforts are essential for ensuring the credibility and applicability of FSM in real-world scenarios.

### B. Determination of Reference SIF

The validation of canopy SIF retrieval in the field poses a considerable challenge due to the inherent difficulty of measuring true SIF. In recent years, different studies have given various solutions. For example, Liu et al. [25] demonstrated the reliability of SIF retrieval results by comparing the consistency between F-SFM retrievals and the outcomes of the 3FLD method. Zhao et al. [27] used the average of the full-spectrum SIF retrieval results from multiple methods as a reference, comparing it with the full-spectrum SIF retrieved from the aFSR method. Chang et al. [46] and Han et al. [47] evaluated the performance of different SIF retrieval methods by examining the relationship between SIF and PAR. Naethe et al. [17] used SFM retrievals as a reference to assess the results of other methods. Wang et al. [48] directly compared the full-spectrum SIF with the single-band results corresponding to different methods. These solutions primarily aim to justify the reasonableness and reliability of the retrieval results by providing a reference.

In this study, our approach is to assess the relative accuracy of the FSM, aFSR, and SpecFit methods while using the SFM SIF as a reference. Initially, the reliability of the SFM method is evaluated through single-band SIF retrieval results based on synthetic data. Comparative analysis with simulated SIF reveals the RMSE values of 0.024 and 0.026 mW/m$^2$/sr/nm for SFM at the $O_2$-A and $O_2$-B bands, respectively, accompanied by RRMSE values of 1.046% and 3.666%. These findings indicate superior or comparable accuracy when compared with the FSM and aFSR methods. Moreover, SFM demonstrates robust and reliable retrieval accuracy in comparison with other single-band SIF retrieval methodologies [47], [49], [50], including the FLD, 3FLD, and iFLD methods. Although alternative methods, such as the 3FLD [25] and iFLD [41] methods, have been deployed in certain studies to evaluate the newly proposed methodologies, it is crucial to note that the inherent assumptions of these two methods do not align with empirical evidence in the $O_2$-B band. Consequently, we have opted to exclusively utilize SFM due to its consistency with objective facts.

From the field measurements, the current findings reveal notable anomalies in the reflectance reconstruction results of the aFSR method at the Italian site, which can be attributed to the under-representation of the training samples. These anomalies eventually lead to errors in the full-spectrum SIF retrieval results. In contrast, the reflectance reconstruction anomalies of the aFSR method were less pronounced in the results achieved from the German site, resulting in a more consistent performance among the SFM, aFSR, and FSM methods in the retrieval outcomes at this site. These observations suggest that when the reflectance training dataset is sufficiently representative, the retrieval results of the three methods should align. The current results from the German site corroborate this notion by demonstrating consistency among these methods. For the Italian site, the difference in retrieval results among the three methods is mainly due to the fact that the aFSR method generated significantly off-reference retrievals due to reflectance reconstruction anomalies associated with the under-representative training samples. In contrast, there was a high degree of agreement between the FSM retrievals and the reference SIF, thus providing a level of assurance regarding the reliability of utilizing SFM SIF as a reference.

## VI. Conclusion

The essence of the FSM approach proposed in this study lies in its utilization of successive summations of Fourier series expansions to approximate reflectance. This approach enables full-spectrum SIF retrieval independent of the reflectance dataset, thus presenting a theoretical advantage over methods reliant on such datasets. Furthermore, the FSM approach addresses the limitations encountered in existing methods such as WAFER and SpecFit by offering reduced computational cost and the capability of retrieving complete full-spectrum SIF.

Sensitivity analyses in this study further highlight the proficiency of the FSM approach in achieving accurate full-spectrum SIF retrieval across a broad range of SR and SNR combinations. However, it is crucial to acknowledge that its retrieval accuracy experiences a significant decline in conditions defined by coarse SR and low SNR combinations, which diminishes markedly in scenarios characterized by coarse SR. Therefore, caution should be exercised when applying FSM in such circumstances.

Furthermore, it is recommended to conduct additional FSM retrieval studies utilizing various sensors and observational targets to explore its generalizability. Such investigations are crucial for advancing basic SIF research, given that FSM significantly mitigates the reliance of full-spectrum SIF retrieval on the reflectance training datasets and demonstrates superior retrieval outcomes from field measurements.

## Acknowledgment

The authors extend their gratitude to Paul Naethe and the team members involved in the AtmoFLEX (4000122454/17/NL/FF/mg) of European Space Agency for sharing the field measurements. In addition, thanks are also extended to three anonymous reviewers for their time and contributions to this article.

## References

[1] Y. Zhang et al., "Model-based analysis of the relationship between sun-induced chlorophyll fluorescence and gross primary production for remote sensing applications," *Remote Sens. Environ.*, vol. 187, pp. 145–155, Dec. 2016.

[2] S. Du et al., "SIFSpec: Measuring solar-induced chlorophyll fluorescence observations for remote sensing of photosynthesis," *Sensors*, vol. 19, no. 13, p. 3009, Jul. 2019.

[3] Y. Zhang et al., "Consistency between sun-induced chlorophyll fluorescence and gross primary production of vegetation in north America," *Remote Sens. Environ.*, vol. 183, pp. 154–169, Sep. 2016.

[4] Y. Zhang, L. Guanter, J. Joiner, L. Song, and K. Guan, "Spatially-explicit monitoring of crop photosynthetic capacity through the use of space-based chlorophyll fluorescence data," *Remote Sens. Environ.*, vol. 210, pp. 362–374, Jun. 2018.

[5] R. Qiu, G. Han, X. Ma, H. Xu, T. Shi, and M. Zhang, "A comparison of OCO-2 SIF, MODIS GPP, and GOSIF data from gross primary production (GPP) estimation and seasonal cycles in North America," *Remote Sens.*, vol. 12, no. 2, p. 258, Jan. 2020.

[6] C. Frankenberg et al., "New global observations of the terrestrial carbon cycle from GOSAT: Patterns of plant fluorescence with gross primary productivity," *Geophys. Res. Lett.*, vol. 38, no. 17, pp. 236–251, Sep. 2011, doi: 10.1029/2011GL048738.

[7] L. Guanter et al., "Retrieval and global assessment of terrestrial chlorophyll fluorescence from GOSAT space measurements," *Remote Sens. Environ.*, vol. 121, pp. 236–251, Jun. 2012.

[8] Y. Sun et al., "Overview of solar-induced chlorophyll fluorescence (SIF) from the orbiting carbon observatory-2: Retrieval, cross-mission comparison, and global monitoring for GPP," *Remote Sens. Environ.*, vol. 209, pp. 808–823, May 2018.

[9] Y. Yoshida et al., "The 2010 Russian drought impact on satellite measurements of solar-induced chlorophyll fluorescence: Insights from modeling and comparisons with parameters derived from satellite reflectances," *Remote Sens. Environ.*, vol. 166, pp. 163–177, Sep. 2015.

[10] J. Joiner et al., "The seasonal cycle of satellite chlorophyll fluorescence observations and its relationship to vegetation phenology and ecosystem atmosphere carbon exchange," *Remote Sens. Environ.*, vol. 152, pp. 375–391, Sep. 2014.

[11] B. Peng et al., "Assessing the benefit of satellite-based solar-induced chlorophyll fluorescence in crop yield prediction," *Int. J. Appl. Earth Observ. Geoinformation*, vol. 90, Aug. 2020, Art. no. 102126.

[12] J. A. Plascyk and F. C. Gabriel, "The Fraunhofer line discriminator MKII—An airborne instrument for precise and standardized ecological luminescence measurements," *IEEE Trans. Instrum. Meas.*, vol. IM-24, no. 4, pp. 306–313, Dec. 1975.

[13] S. W. Maier, K. P. Gunther, and M. Stellmes, "Sun-induced fluorescence: A new tool for precision farming," *Digital Imag. Spectral Techn., Appl. Precis. Agricult. Crop Physiol.*, vol. 66, pp. 207–222, 2004, doi: 10.2134/asaspecpub66.c16.

[14] L. Alonso et al., "Improved Fraunhofer line discrimination method for vegetation fluorescence quantification," *IEEE Geosci. Remote Sens. Lett.*, vol. 5, no. 4, pp. 620–624, Oct. 2008.

[15] X. Liu and L. Liu, "Improving chlorophyll fluorescence retrieval using reflectance reconstruction based on principal components analysis," *IEEE Geosci. Remote Sens. Lett.*, vol. 12, no. 8, pp. 1645–1649, Aug. 2015.

[16] M. Meroni and R. Colombo, "Leaf level detection of solar induced chlorophyll fluorescence by means of a subnanometer resolution spectroradiometer," *Remote Sens. Environ.*, vol. 103, no. 4, pp. 438–448, Aug. 2006.

[17] P. Naethe et al., "A precise method unaffected by atmospheric reabsorption for ground-based retrieval of red and far-red sun-induced chlorophyll fluorescence," *Agricult. Forest Meteorol.*, vol. 325, Oct. 2022, Art. no. 109152.

[18] Y. Zhang et al., "ChinaSpec: A network for long-term ground-based measurements of solar-induced fluorescence in China," *J. Geophys. Res., Biogeosci.*, vol. 126, no. 3, Mar. 2021, Art. no. e2020JG006042, doi: 10.1029/2020JG006042.

[19] C. Buschmann, "Variability and application of the chlorophyll fluorescence emission ratio red/far-red of leaves," *Photosynthesis Res.*, vol. 92, no. 2, pp. 261–271, Aug. 2007.

[20] A. A. Z. Malenovský, J. Olejníčková, A. Gallé, U. Rascher, and G. Mohammed, "Meta-analysis assessing potential of steady-state chlorophyll fluorescence for remote sensing detection of plant water, temperature and nitrogen stress," *Remote Sens. Environ.*, vol. 168, pp. 420–436, Oct. 2015.

[21] E. Middleton et al., "The 2013 FLEX—U.S. airborne campaign at the parker tract loblolly pine plantation in North Carolina, USA," *Remote Sens.*, vol. 9, no. 6, p. 612, Jun. 2017.

[22] J. Verrelst et al., "Evaluating the predictive power of sun-induced chlorophyll fluorescence to estimate net photosynthesis of vegetation canopies: A SCOPE modeling study," *Remote Sens. Environ.*, vol. 176, pp. 139–151, Apr. 2016.

[23] G. H. Mohammed et al., "Remote sensing of solar-induced chlorophyll fluorescence (SIF) in vegetation: 50 years of progress," *Remote Sens. Environ.*, vol. 231, Sep. 2019, Art. no. 111177.

[24] F. Zhao, Y. Guo, W. Verhoef, X. Gu, L. Liu, and G. Yang, "A method to reconstruct the solar-induced canopy fluorescence spectrum from hyperspectral measurements," *Remote Sens.*, vol. 6, no. 10, pp. 10171–10192, Oct. 2014.
[25] X. Liu, L. Liu, S. Zhang, and X. Zhou, "New spectral fitting method for full-spectrum solar-induced chlorophyll fluorescence retrieval based on principal components analysis," *Remote Sens.*, vol. 7, no. 8, pp. 10626–10645, Aug. 2015.
[26] S. Cogliati et al., "Retrieval of sun-induced fluorescence using advanced spectral fitting methods," *Remote Sens. Environ.*, vol. 169, pp. 344–357, Nov. 2015.
[27] F. Zhao et al., "Reconstruction of the full spectrum of solar-induced chlorophyll fluorescence: Intercomparison study for a novel method," *Remote Sens. Environ.*, vol. 219, pp. 233–246, Dec. 2018.
[28] W. Verhoef and H. Bach, "Simulation of Sentinel-3 images by four-stream surface–atmosphere radiative transfer modeling in the optical and thermal domains," *Remote Sens. Environ.*, vol. 120, pp. 197–207, May 2012.
[29] W. Verhoef, C. van der Tol, and E. M. Middleton, "Hyperspectral radiative transfer modeling to explore the combined retrieval of biophysical parameters and canopy fluorescence from FLEX–Sentinel-3 tandem mission multi-sensor data," *Remote Sens. Environ.*, vol. 204, pp. 942–963, Jan. 2018.
[30] C. van der Tol, W. Verhoef, J. Timmermans, A. Verhoef, and Z. Su, "An integrated model of soil-canopy spectral radiances, photosynthesis, fluorescence, temperature and energy balance," *Biogeosciences*, vol. 6, no. 12, pp. 3109–3129, Dec. 2009.
[31] P. Yang, E. Prikaziuk, W. Verhoef, and C. van der Tol, "SCOPE 2.0: A model to simulate vegetated land surface fluxes and satellite signals," *Geosci. Model Develop.*, vol. 14, no. 7, pp. 4697–4712, Jul. 2021.
[32] A. Berk, "MODTRAN5: A reformulated atmospheric band model with auxiliary species and practical multiple scattering options," *Proc. SPIE*, vol. 5425, pp. 341–347, Aug. 2005.
[33] L. Liu, X. Liu, and J. Hu, "Effects of spectral resolution and SNR on the vegetation solar-induced fluorescence retrieval using FLD-based methods at canopy level," *Eur. J. Remote Sens.*, vol. 48, no. 1, pp. 743–762, Jan. 2015.
[34] Z. Ni et al., "Investigation of atmospheric effects on retrieval of sun-induced fluorescence using hyperspectral imagery," *Sensors*, vol. 16, no. 4, p. 480, Apr. 2016.
[35] S. Du, L. Liu, X. Liu, X. Zhang, X. Gao, and W. Wang, "The solar-induced chlorophyll fluorescence imaging spectrometer (SIFIS) onboard the first terrestrial ecosystem carbon inventory satellite (TECIS-1): Specifications and prospects," *Sensors*, vol. 20, no. 3, p. 815, Feb. 2020.
[36] W. Verhoef and H. Bach, "Simulation of hyperspectral and directional radiance images using coupled biophysical and atmospheric radiative transfer models," *Remote Sens. Environ.*, vol. 87, no. 1, pp. 23–41, Sep. 2003.
[37] W. Verhoef, C. Van der Tol, and E. M. Middleton, "Vegetation canopy fluorescence and reflectance retrieval by model inversion using optimization," in *Proc. 5th Int. Workshop Remote Sens. Vegetation Fluorescence*, Apr. 2014, pp. 22–24.
[38] F. Zhao et al., "Retrieval of red solar-induced chlorophyll fluorescence with TROPOMI on the Sentinel-5 precursor mission," *IEEE Trans. Geosci. Remote Sens.*, vol. 60, pp. 1–14, 2022, doi: 10.1109/TGRS.2022.3162726.
[39] P. Köhler, L. Guanter, and J. Joiner, "A linear method for the retrieval of sun-induced chlorophyll fluorescence from GOME-2 and SCIAMACHY data," *Atmos. Meas. Techn.*, vol. 8, no. 6, pp. 2589–2608, 2015.
[40] M. Meroni et al., "Remote sensing of solar-induced chlorophyll fluorescence: Review of methods and applications," *Remote Sens. Environ.*, vol. 113, no. 10, pp. 2037–2051, Oct. 2009.
[41] V. Oehl and A. Damm, "WAFER: A new method to retrieve sun-induced fluorescence based on spectral wavelet decompositions," *Remote Sens. Environ.*, vol. 298, Dec. 2023, Art. no. 113786.
[42] R. Scodellaro et al., "A novel hybrid machine learning phasor-based approach to retrieve a full set of solar-induced fluorescence metrics and biophysical parameters," *Remote Sens. Environ.*, vol. 280, Oct. 2022, Art. no. 113196.
[43] S. Cogliati et al., "A spectral fitting algorithm to retrieve the fluorescence spectrum from canopy radiance," *Remote Sens.*, vol. 11, no. 16, p. 1840, Aug. 2019.
[44] J. P. Gastellu-Etchegorry, E. Martin, and F. Gascon, "DART: A 3D model for simulating satellite images and studying surface radiation budget," *Int. J. Remote Sens.*, vol. 25, no. 1, pp. 73–96, Jan. 2004.
[45] F. Zhao et al., "FluorWPS: A Monte Carlo ray-tracing model to compute sun-induced chlorophyll fluorescence of three-dimensional canopy," *Remote Sens. Environ.*, vol. 187, pp. 385–399, Dec. 2016.
[46] C. Y. Chang et al., "Systematic assessment of retrieval methods for canopy far-red solar-induced chlorophyll fluorescence using high-frequency automated field spectroscopy," *J. Geophys. Res., Biogeosci.*, vol. 125, no. 7, Jul. 2020, Art. no. e2019JG005533, doi: 10.1029/2019JG005533.
[47] S. Han et al., "Using high-frequency PAR measurements to assess the quality of the SIF derived from continuous field observations," *Remote Sens.*, vol. 14, no. 9, p. 2083, Apr. 2022.
[48] R. Wang et al., "Harmonizing solar induced fluorescence across spatial scales, instruments, and extraction methods using proximal and airborne remote sensing: A multi-scale study in a soybean field," *Remote Sens. Environ.*, vol. 281, Nov. 2022, Art. no. 113268.
[49] X. Zhou, Z. Liu, S. Xu, W. Zhang, and J. Wu, "An automated comparative observation system for sun-induced chlorophyll fluorescence of vegetation canopies," *Sensors*, vol. 16, no. 6, p. 775, May 2016.
[50] M. P. Cendrero-Mateo et al., "Sun-induced chlorophyll fluorescence III: Benchmarking retrieval methods and sensor characteristics for proximal sensing," *Remote Sens.*, vol. 11, no. 8, p. 962, Apr. 2019.

**Shilei Li** (Member, IEEE) received the Ph.D. degree in agricultural remote sensing from the Institute of Agricultural Resources and Regional Planning, Chinese Academy of Agricultural Sciences, Beijing, China, in 2024.

He is currently a Post-Doctoral Fellow at the State Key Laboratory of Efficient Utilization of Arid and Semi-Arid Cropland in Northern China, Institute of Agricultural Resources and Agricultural Planning, Chinese Academy of Agricultural Sciences. His research interests include retrieval of Sun-induced chlorophyll fluorescence (SIF) from ground, airborne, and satellite platforms as well as applied analyses of ecosystems, crop growth status, and crop yields based on SIF data.

**Maofang Gao** (Senior Member, IEEE) was born in Shandong, China. She received the bachelor's degree in geography from Northeast Normal University, Changchun, Jilin, China, in 2003, the master's degree in cartography and geography information system from Nanjing University, Nanjing, China, in 2006, and the Ph.D. degree in agricultural remote sensing from Chinese Academy of Agricultural Sciences, Beijing, China, in 2011.

Since 2006, she has been a Research Staff Member at the Institute of Agricultural Resources and Regional Planning, Chinese Academy of Agricultural Sciences, where she has been a Professor since 2023. Her research interests include quantitative remote sensing and agricultural drought monitoring.

**Zhao-Liang Li** (Fellow, IEEE) received the Ph.D. degree in terrestrial environmental physics from the University of Strasbourg, Strasbourg, France, in 1990.

Since 1992, he has been a Research Scientist at CNRS, Illkirch, Strasbourg. He joined the Institute of Agricultural Resources and Regional Planning, Chinese Academy of Agricultural Sciences, Beijing, China, in 2012. He has participated in many national and international projects, including NASA-funded Moderate Resolution Imaging Spectroradiometer (MODIS), the EC-funded EAGLE Program, and various ESA-funded initiatives such as SPECTRA. His main areas of expertise include thermal infrared radiometry, parameterization of land surface processes at a large scale, and the assimilation of satellite data to land surface models.

**Jélila Labed** received the Ph.D. degree in physics of terrestrial environment in the thermal infrared domain from the University of Strasbourg, Strasbourg, France, in 1990.

She passed a national competitive examination in 1991 and has since been working as an Associate Professor at the University of Strasbourg. From 2005 to 2010, she served as the Director of Studies at the School of Physics, Telecom Physique Strasbourg, University of Strasbourg. Since 2010, she has been teaching engineering project management in addition to experimental physics. She has organized and participated in many field campaigns in different countries and has published over 40 publications in international peer-reviewed journals. Her research interests include radiometry in the thermal infrared domain as applied to terrestrial surfaces and modeling land surface processes at a large scale—particularly the estimation of land surface temperature and evapotranspiration from satellite data and urban climatology.

**Wouter Verhoef** received the Ing. degree in physics engineering from the Technical College of Dordrecht, Dordrecht, The Netherlands, in 1972, and the Ph.D. degree in agricultural and environmental sciences from Wageningen University, Wageningen, The Netherlands, in 1998, focusing on radiative transfer modeling in vegetation canopies and the atmosphere.

He started his career in optical remote sensing at the Netherlands Interdepartmental Working Community for the Application of Remote Sensing Techniques (NIWARS), Delft, The Netherlands, where he was involved in a field spectrometer measurement program focused on vegetation, soils, and water. In 1977, he joined the National Aerospace Laboratory (NLR), The Netherlands, where he developed the widely known SAIL canopy reflectance model in 1981, along with several improved variants. At NLR, he also created image processing methodologies for time-series analysis (HANTS algorithm) and a wavelet-based data compression algorithm for hyperspectral images. He participated in several European Space Agency (ESA) studies in preparation for a multangular hyperspectral Earth Explorer Mission. In 2005, he contributed to the ESA-China DRAGON Program by delivering 12 lectures in Beijing, China, and he was appointed as a Visiting Professor at Capital Normal University, Beijing. Since May 2006, he has held a 30% visiting professor position at the International Institute for Geoinformation Science and Earth Observation, Enschede, The Netherlands. He retired from the Faculty of Geo-Information Science and Earth Observation (ITC), University of Twente, Enschede, in 2016.

Dr. Verhoef was a member of ESA's FLEX Mission Assessment Group.